Numerical modeling of the ultrafast plasmonic response of titanium nitride nanostructures

Silvia Rotta Loria,[†,‡] Andrea Schirato,[†,¶] Giulia Crotti,[†] Unai Arregui Leon,[†] Bruno Palpant,[‡] Margherita Zavelani-Rossi,[*,§,‖] and Giuseppe Della Valle[*,†,‖,⊥]

†*Dipartimento di Fisica, Politecnico di Milano, Piazza Leonardo da Vinci, 32, I-20133 Milano, Italy*

‡*Université Paris-Saclay, CNRS, ENS Paris-Saclay, CentraleSupélec, LuMIn, Gif-sur-Yvette, France*

¶*Department of Physics and Astronomy, Rice University, Houston, Texas 77005, United States*

§*Dipartimento di Energia - Politecnico di Milano, Via Ponzio 34/3, I-20133 Milano, Italy*

‖*Istituto di Fotonica e Nanotecnologie - Consiglio Nazionale delle Ricerche, Piazza Leonardo da Vinci, 32, I-20133 Milano, Italy*

⊥*Istituto Nazionale di Fisica Nucleare - Sezione di Milano, Via Celoria, 16, I-20133 Milano, Italy*

E-mail: margherita.zavelani@polimi.it; giuseppe.dellavalle@polimi.it

Abstract

Titanium Nitride (TiN) is a promising plasmonic material which has come into the spotlight as a valid alternative to noble metals. As for other plasmonic materials, great attention has been given to the development of TiN nanostructures so as to efficiently tune the plasmon resonance, also combining them in lattices and with other metals or semiconductors. In addition, TiN boasts a carrier cooling dynamics more than one order of magnitude faster than that of gold, which gives it a clear advantage in many applications. However, the knowledge of the ultrafast optical response of TiN nanostructures is narrowed down to experimental evidence, without a complete modeling. In this work, we numerically model the nonequilibrium hot-carrier-mediated mechanisms and ultrafast nonlinear changes in the optical response of TiN nanostructures photoinduced by femtosecond laser pulses. Specifically, we focus on nanodisks and nanospheres, and we compare our simulations with experimental pump-probe measurements. Our approach enables us to disentangle the interband and intraband contributions to the permittivity modulation, pointing out the critical role of the interplay between the TiN interband transitions and the nanostructure optical resonances in the early stages of the photoinduced ultrafast dynamics.

Introduction

When light interacts with plasmonic nanoparticles, the conduction electrons of the metal can support driven collective oscillations, resonantly generating a localized surface plasmon (LSP). The LSP is able to localize and enhance the electromagnetic field within subwavelength spatial regions. This peculiar property is exploited in a variety of applications such as sensing, nanoscale imaging and surface-enhanced spectroscopies, to mention a few.[1] Recently, plasmonic nanostructures have also attracted notable interest due to the strong nonlinear optical effects that arise when these metal nano-objects interact with an intense laser pulse.[2,3] Indeed, nanostructured metals are much more advantageous for nonlinear op-

tics applications as compared with their bulk counterpart, being transparent in a broad frequency range, and capable of boosting nonlinear effects at the LSP resonances. Moreover, the plasmonic field confinement enables to exploit these processes into photonic devices of nanometric dimensions.[4,5] A further advantage of nanostructures compared to the bulk is the enhanced photogeneration of out-of-equilibrium 'hot' charge carriers,[6] due to the higher surface-to-volume ratio. In turn, these photoexcited electrons preside over giant third-order optical nonlinearities, dominating the system response in the transient regime.[7] A whole branch of plasmonics, referred to as ultrafast plasmonics, has developed to investigate these phenomena and explain the origin and relaxation mechanisms of hot carriers in plasmonic nanostructures.[8–11]

From the material standpoint, noble metals (Au, Ag, Cu) have largely been, to date, the main candidates for the study and development of plasmonic nanostructures. However, despite their high conductivity and malleability, they present major drawbacks, such as a low melting temperature (especially when downsized to the nanoscale), CMOS incompatibility, and hardly adjustable optical properties.[12] In the last decade, titanium nitride (TiN) has emerged as one of the most promising alternative materials in this regard.[13,14] Indeed, it melts at ~ 3000 °C,[15] making it ideal for high-temperature applications,[16,17] and its dielectric properties can be modified by acting on the stoichiometry during fabrication.[18] In addition, TiN shows good biocompatibility and chemical stability, no diffusion in silicon, interband losses lower than in Au at optical frequencies, and its plasmonic resonance typically covers a wide spectral range in the visible and near infrared (IR).[18,19] For what concerns fabrication, on the one hand 2D-lattices of TiN nanostructures can be easily built from the patterning of compact TiN films through lithography methods as electron beam lithography, laser writing, or etching,[14] also reaching large scale systems, a major advantage for practical applications.[20] On the other hand, to fabricate TiN nanoparticles in solution, typical techniques are direct nitridation of titanium or titanium dioxide, urea route, and vapour synthesis.[14] TiN nanoantennas find applications in many different fields, such as thermoplasmonics,[21–23] catalysis,[24,25]

energy storage,[26] solar concentrators,[27] plasmonic photothermal therapy,[28] surface-enhanced Raman scattering,[29] and heat-assisted magnetic recording.[30] Following the rapidly increasing interest towards TiN nanoparticles, many research groups have thoroughly investigated their stationary optical response in the last years. TiN presents a prominent metallic character, although its band structure is typical of a highly doped semiconductor.[31–34] Contrarily, only a limited number of experimental works have been dedicated to exploring the ultrafast optical response of TiN nanostructures,[35–37] and a rigorous numerical description of carrier relaxation in these structures is still missing. This is a major lack, especially considering that TiN exhibits, in the ultrafast regime, substantial differences compared to more conventional plasmonic materials. Indeed, TiN hot electrons equilibrate extremely fast with the lattice, in less than $\sim$ 100 fs, i.e., more than 10 times faster than in noble metals.[38,39] Combined with this peculiar dynamics, the giant optical nonlinearity mediated by the photoinduced hot carriers in TiN could enable an easy scalability of optoelectronic devices, leading to high efficiencies in architectures featuring nanometric dimensions. Moreover, the study of novel materials with epsilon-near-zero (ENZ) properties in the optical frequency range, such as TiN, is crucial to develop new technologies boasting enhanced nonlinear optical interactions. This property is highly desirable when aiming to realize new devices for the all-optical modulation of light.[40–42]

In this work, we model the ultrafast optical response of TiN nanostructures upon photoexcitation with fs-laser pulses, implementing substantial modifications to the calculations developed for TiN films.[39] Indeed, describing the transient optical response of nanostructures supporting geometrically-induced optical resonances requires to account for nontrivial effects such as a different heat dissipation in the structure and possible skin effects peculiar to each shape and dimension of the nano-object, in addition to the appropriate description of the nanostructure stationary optical features. Our model is directly compared and validated over relevant experimental data obtained by femtosecond pump-probe spectroscopy available in the literature. Specifically, we refer to two experimental studies, on TiN nan-

odisks[36] and colloidal TiN nanospheres,[37] respectively, which both measure the nanostructures' ultrafast response, yet without providing a quantitative explanation for the optical phenomena observed. Starting from a system of two coupled, first order differential equations, the two-temperature model (2TM), combined with a semiclassical modeling of TiN optical transitions, we are able to determine how the optical properties of TiN nanostructures are transiently modified upon ultrafast laser excitation, and to highlight the key role of the hot carrier energy distribution depending on the nanostructure shape. Our findings are crucial to provide a comprehensive understanding of the optical nonlinearities of TiN nanostructures, paving the way to realize new TiN-based devices for ultrafast plasmonics applications.

Results and discussion

The first structure we analyze in this work consists of a square lattice of TiN nanodisks on a sapphire substrate in air, investigated in the work by Reese *et al.*[36] The disks have diameter $d_d = 200$ nm, height $h = 50$ nm, and the lattice has periodicity $P = 600$ nm. In our calculations, we approximate this system as a random ensemble of TiN disks, spatially dispersed in a matrix having a refractive index close to the mean value between the ones of glass and air. The second structure considered is a colloidal aqueous solution of TiN nanospheres of diameter $d_s = 50$ nm, reported in the work by Adhikari *et al.*[37] In order to study the origin of the ultrafast optical nonlinearities in these nanostructures, we start by modeling their stationary optical response. To do so, we cannot rely on the bare quasi-static theory (QST). Indeed, the latter is an analytical theory that enables to retrieve the polarizability of nanoparticles under the approximation of constant phase of the electric field in space. Therefore, it applies when the dimension of the nano-object is much smaller than the wavelength of light, i.e., for sizes typically below ∼30 nm in the visible/near-infrared spectrum.[43] We resort instead to an analytical extended formulation of the QST including

retardation effects[44] for the relatively large nanostructures under scrutiny. Specifically, we take into account retardation effects by including in the particle polarizability a size factor $s = \sqrt{\varepsilon_h}L/\lambda$, depending on the permittivity of the host medium ε_h, a characteristic size of the particle L, and the wavelength of the incident light λ. The modified polarizability of the nanoparticle can then be written as:[44]

$$\alpha(\omega) = \frac{\varepsilon_h}{4\pi} \sum_j V_j \left(\frac{1}{\varepsilon_m/\varepsilon_h - 1} - \frac{1}{\varepsilon_j - 1} - A_j(s) \right)^{-1} \tag{1}$$

where j is the index of a specific electrostatic mode volume V_j and $\sum_j V_j = V$, the physical volume of the nanoparticle. Moreover, $A_j(s) = a_{j2}s^2 + 4\pi^2 i V_j/(3L^3)s^3 + a_{j4}s^4$ is an s- dependent function expanded up to the fourth order, ε_m is the metal permittivity, a_{j2}, a_{j4} and ε_j are real numerical constants dependent on the nanoparticle shape and volume only.[44] With the so-obtained polarizability, we can evaluate the stationary absorption, scattering and extinction cross sections of the nanoparticles under investigation. Details of the cross sections' calculations are reported in Methods (Eq. 7 and Eq. 8). The simulated cross sections of absorption, scattering and extinction are shown (blue dotted, light-blue dashed and green solid curves) for nanodisks and nanospheres in Figs. 1a and 1b, respectively. For nanodisks, we notice two distinct peaks in the cross sections. The peak at longer wavelengths (at around 1150 nm) is larger in amplitude and related to the two degenerate LSP modes polarized parallel to the nanodisk bases, while the one at shorter wavelengths ($\sim$450 nm) is due to the transversal mode (i.e., along the disk height direction). In the case of the nanospheres, we have instead one peak, at $\sim$625 nm, due to the threefold mode degeneracy. We can then calculate the stationary transmission spectra for the nanostructure ensembles as $T = T_{fr} \exp\left(-\sigma_{ext}(\lambda)N\right)$. For the nanodisks, T_{fr} is the Fresnel transmission at the air-glass interface and $N = 1/P^2$ is the number of nanodisks per area unit. In the case of nanospheres, we neglect any interface ($T_{fr} = 1$) and $N = c_{exp}N_A L$, where $c_{exp} = 0.11 \times 10^{-6}$ mol m^{-3} is the experimental concentration of TiN nanospheres in the solution, kept as a fitting parameter

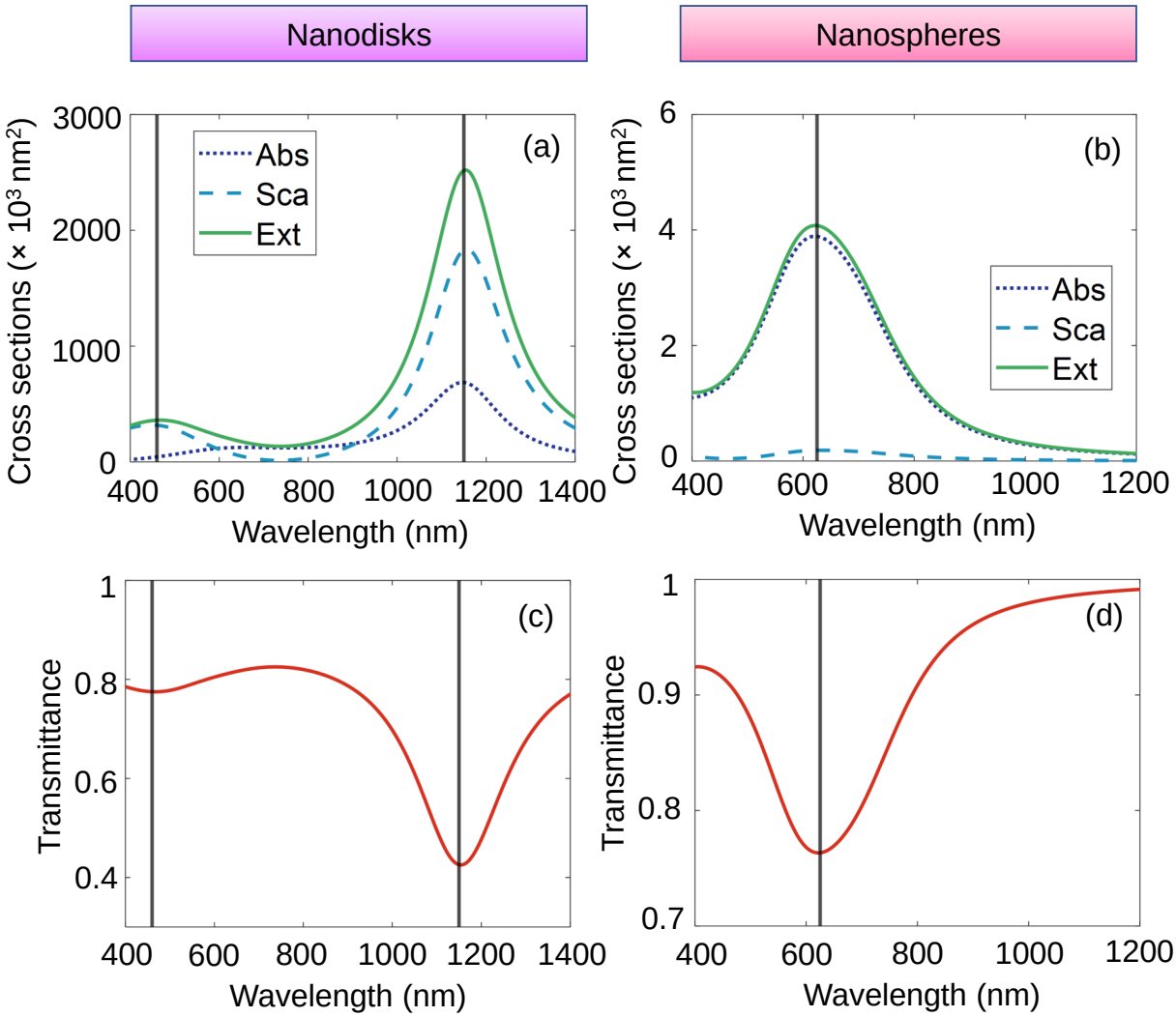

Figure 1: Stationary absorption, scattering and extinction cross sections (blue dotted, light-blue dashed and green curves, respectively) for a) disks with parameters $h = 50$ nm and $d_d = 200$ nm in a matrix with refractive index close to the mean between the ones of sapphire and air (see Methods), so as to simulate the squared lattice of TiN nanodisks on a sapphire substrate and in air as in Ref. [36], and b) nanospheres with diameter $d_s = 50$ nm in water as in Ref. [37]. Cross sections are computed for single scatterers. Transmittance spectrum for a random ensemble of the same c) nanodisks and d) nanospheres. Vertical black lines mark the spectral position of the plasmonic resonance peaks.

since not provided in the experimental work,[37] N_A is the Avogadro's number, and $L = 1$ mm is the typical cuvette length. The transmission spectrum for nanodisks is displayed in Fig. 1c, with a marked dip at ∼1150 nm and a weaker one at ∼460 nm, and for nanospheres in Fig. 1d, where the dip falls at ∼625 nm. Both results are in good agreement with previous experimental reports[33,36,37] on comparable systems. The presence of two peaks in the case of nanodisks, which experimentally show only the resonance at longer wavelengths upon normal incidence excitation of the 2D array,[36] stems from the approximation of the sample to a disordered ensemble of particles. Besides this aspect, the discrepancies in the stationary response of the nanodisks between our simulations and the measured spectrum can be mainly attributed to the approximated shape and environment of the simulated system. For the nanospheres, slight mismatches may be due to the values of the dielectric permittivity constants, that were assimilated to the ones of epitaxially grown TiN films.[33] The TiN permittivity data employed in our model are reported in the Supporting Information (SI).

To study the delayed nonlinear optical response of plasmonic nanostructures, ultrafast pump-probe spectroscopy is a widespread, powerful tool. We thus aim at validating our theoretical model on the experimental measurements reported in the selected works. The measured signal maps taken from Refs. [36] and [37] are shown in Figs. 2a and 2c, respectively. The pump-probe signal retrieved in both experiments is the differential absorbance $\Delta A(\lambda, t) = A_{exc}(\lambda, t) - A_0(\lambda)$, where $A_{exc}(\lambda, t)$ is the time-dependent absorbance of the excited sample upon ultrafast illumination, and $A_0(\lambda)$ is its absorbance in stationary conditions. In the case of nanodisks, the sample is pumped with a 800-nm pulse from a Ti:Sapphire laser with 35-fs duration and 1 kHz repetition rate. The experimental pump fluence is set to $F = 1.5$ mJ cm^{-2}. The ultrafast optical response is then probed over a broad spectral range in the near IR, from 950 nm to 1400 nm, and along a temporal delay up to 1 ns after the pump interaction with the sample. The experimental ΔA map (Fig. 2a) shows a strong negative signal close to the LSP wavelength, and a weak positive signal at its edges (for $\lambda >$ ∼1200 nm and a weaker one for $\lambda <$ ∼1080 nm). The latter is ascribed to the resonance

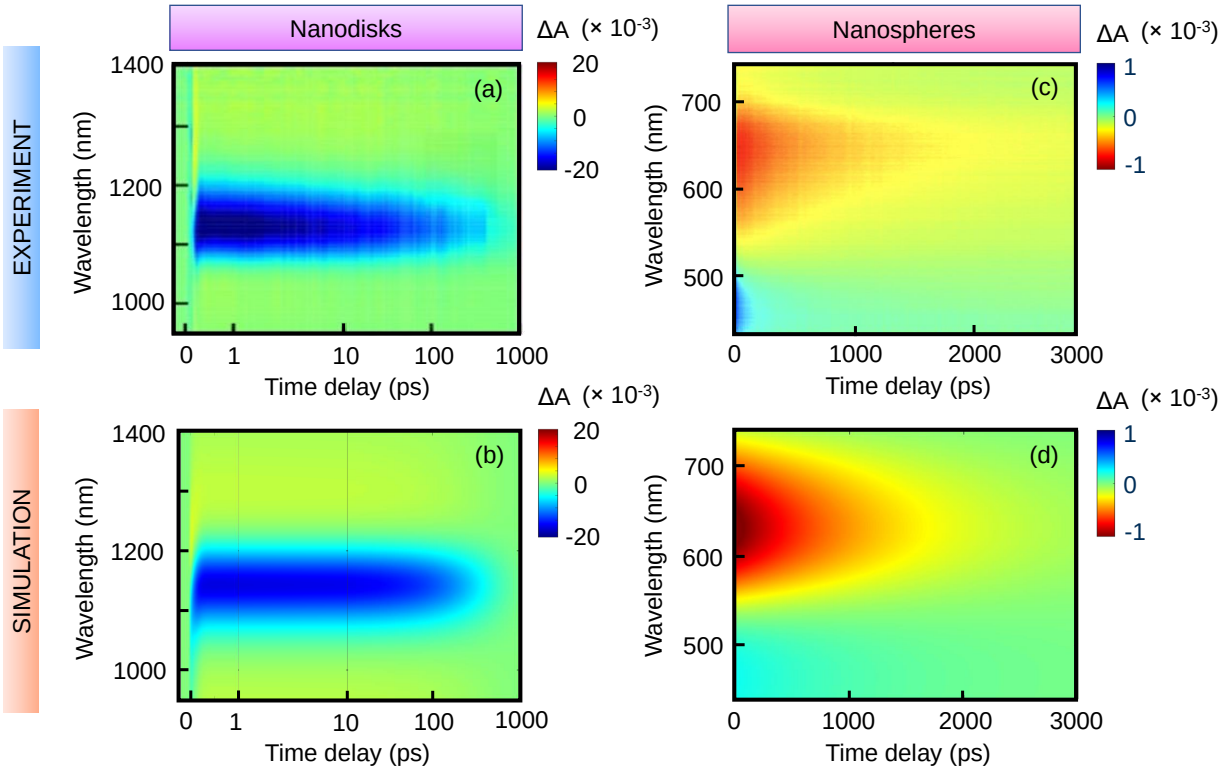

Figure 2: a) Experimental and b) simulated pump–probe map of differential transient absorbance for TiN nanodisks. Pump wavelength: 800 nm, pump pulse temporal duration: 35 fs, pump fluence (simulation): 2.25 mJ cm^{-2}. Red for positive signal, blue for negative signal. c) Experimental and d) numerical pump–probe map for TiN nanospheres in water. Pump wavelength: 900 nm, pump pulse duration: 130 fs, pump fluence (simulation): 336 μJ cm^{-2}. Blue for positive signal, red for negative signal. a) Adapted with permission from Ref. [36], Copyright 2021, American Chemical Society. c) Adapted with permission from Ref. [37], Copyright 2021, American Physical Society.

broadening, as a consequence of the ultrafast nanoparticle's heating.[36] For what concerns the nanospheres, less experimental details are provided in the original publication.[37] The sample is pumped with a 900-nm pulse from a Ti:Sapphire laser with a pulse duration of 130 fs, and probed with a white supercontinuum covering a broad portion of the visible range (440-740 nm), spanning a time delay between pump and probe up to 3 ns. The pump-probe map (Fig. 2c) shows a broad negative signal (note the color scale inversion among the two experimental plots in Figs. 2a and 2c), which lasts for almost 2 ns. There is also a weak positive signal at wavelengths below 500 nm. The whole response is interpreted as a mere blue-shift of the plasmonic resonance.[37] For a theoretical description of the observed transient optical behaviors, we model the ultrafast photoexcitation by means of the two-temperature model (2TM), a thermodynamical model stemming from the Boltzmann equation.[45] When an ultrafast laser pulse interacts with a metallic nanoparticle, the quasi-free carrier plasma reaches nonequilibrium states (associated with higher electronic temperature), and subsequently equilibrates with and heats up the lattice. Finally, the latter releases heat towards the surrounding environment. The 2TM describes these energy exchanges through two coupled differential equations at the first order, assuming both the carrier and the phonon baths at internal thermal equilibrium at each time instant. In this approach, the short-lived nonthermal regime for the electron gas is disregarded, due to the extremely short electron-electron scattering time in this material,[38,39] and diffusion terms for electrons and phonons are neglected due to the small dimensions of the nanoparticles. Eq. 2 details the increase in the carrier temperature T_C, following the absorption of the instantaneous pump power density P_A (see SI, Section S2), while Eq. 3 accounts for the evolution of the lattice temperature T_L:

$$C_C \frac{\mathrm{d}T_C}{\mathrm{d}t} = -G(T_C - T_L) + P_A(t) \tag{2}$$

$$C_L \frac{\mathrm{d}T_L}{\mathrm{d}t} = G(T_C - T_L) - G_L(T_L - T_0) \tag{3}$$

where $C_C = \gamma T_C$ and C_L are the carrier and lattice heat capacities, respectively, γ is the carrier heat capacity constant, T_0 is the room temperature, G and G_L are the carrier-lattice and the lattice-environment coupling coefficients, respectively. The latter embeds the heat transfer from the phonon bath to the external environment, taking into account the geometry of the nanoparticle and the thermal conditions at the boundary between the two media. It needs to be fitted on experimental data.[46] The values for $C_L = 3.149 \times 10^6$ J m^{-3} K^{-1}, $\gamma = 112.5$ J m^{-3} K^{-2} and $G = 10^{18}$ W m^{-3} K^{-1} are the same as those used for TiN films.[39] For G_L, the best fitting values turned out to be $G_{L,disk} = 10^{16}$ W m^{-3} K^{-1} and $G_{L,sphere} = 0.27 \times 10^{16}$ W m^{-3} K^{-1}, for the disks and for the spheres, respectively. The higher value of G_L in the case of the disks is due to the presence of a solid-state substrate, inducing a more efficient heat dissipation towards the environment, compared to the case of the spheres, being dispersed in water. In Fig. 3, we report the temporal evolution of the carrier and lattice temperatures

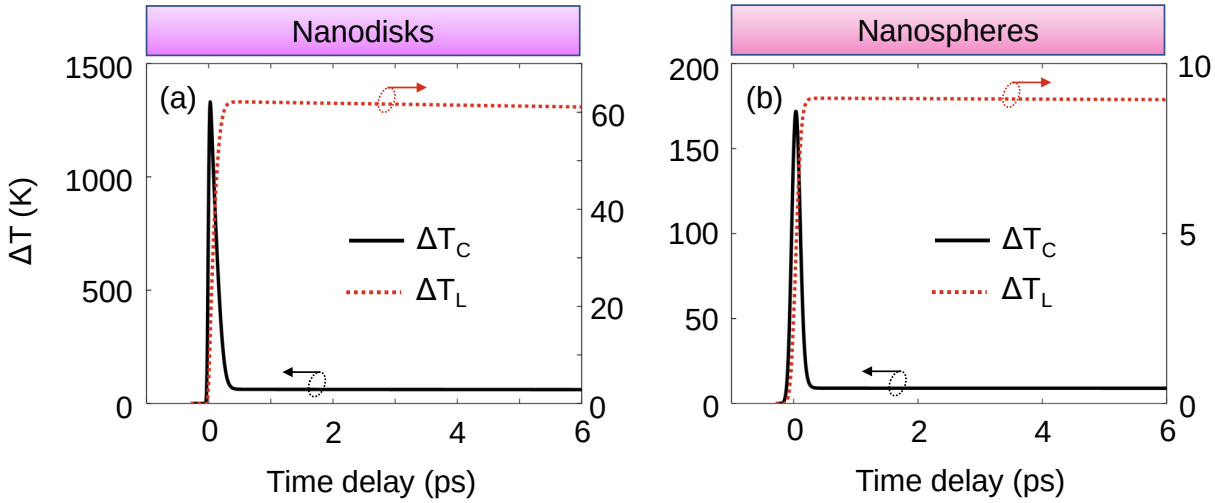

Figure 3: Temporal evolution of the carrier and lattice temperatures with respect to the room temperature (solid black and red dotted curves, respectively) for TiN a) nanodisks and b) nanospheres, retrieved from the 2TM. Pump fluences as in Figs. 2b and 2d.

for nanodisks (Fig. 3a) and nanospheres (Fig. 3b) retrieved from the 2TM. When the pump pulse interacts with the TiN nanostructures, the electron gas heats up, reaching a maximum temperature variation of about 1330 K for nanodisks and 170 K for nanospheres in the respective conditions of the corresponding experiments. The difference in the maximum

temperature reached is mostly due to the different excitation levels. Indeed, the absorbed pump fluence is higher for disks than for spheres, as a combination of higher incident fluence and higher absorption cross section. After the pump excitation, the hot carriers start to relax extremely fast towards the lattice, in line with what proved for TiN,[38,39,47] returning close to T_0 within ∼410 fs for nanodisks, ∼320 fs for nanospheres. The slower relaxation of hot electrons in nanodisks finds reason in the dependence of the carrier heat capacity C_C on the electronic temperature T_C, and it is physically caused by the increase in the electron thermal inertia at high fluences.[48] The lattice temperature grows simultaneously with the energy release from the carriers to the phonon bath, reaching a plateau of ΔT_L ∼62 K in ∼340 fs for nanodisks and of ΔT_L ∼9 K in ∼250 fs for nanospheres. At the plateau, the thermal equilibrium between the carrier and the phonon populations is reached, as $T_C = T_L$. As a consequence of photon absorption, the Fermi distribution of electrons (initially at T_0) is perturbed, and reaches a nonequilibrium state described by a higher temperature T_C. Empty (occupied) states are created below (above) the Fermi level in the conduction band. This phenomenon is known as Fermi smearing,[49] and in formulas it can be expressed as the difference between the Fermi electronic distribution f_0 at the hot carrier temperature T_C and the one at T_0:

$$\Delta f(E,t) = f_0[E, T_C(t)] - f_0[E, T_0] \tag{4}$$

where E is the energy of the carriers. The modified electronic distribution translates in turn into variations of the material optical properties: some interband transitions involving final states below (above) the Fermi level become possible (hindered). To include such effects in our model, we consider a few approximations in the description of TiN band structure.[39] We account for one interband transition only to be affected by the pump pulse absorption, namely the one at the Γ point of the Brillouin zone, from the upper valence band to the half-filled conduction band ($\Gamma_{15} \rightarrow \Gamma_{25'}$, see Ref. 34 for details), also assuming perfect parabolicity of the bands around Γ. In the vicinity of this point, the value of the hole effective mass m_h is taken in agreement with what found for TiN films[39] ($m_h = 1.2 m_{h,film}$). The effective electron

mass m_e is kept, instead, as a fitting parameter, since the curvature of the conduction band around Γ is very sensitive to the composition of the TiN sample, and to its oxidation level.[47] We set $m_{e,disk} = 4m_{e,film}$ and $m_{e,sphere} = 2m_{e,film}$, in agreement with the progressive nitrogen increase in the TiN composition,[47] moving in order, for the samples we consider, from the films, to the nanospheres and then to the nanodisks, as shown from a progressive red-shift in the plasma wavelength.[39] Indeed, higher nitrogen contents lead to a flattening of the TiN conduction band around Γ. Moreover, the energy gap at the Γ point is set to $E_0 = 2.95$ eV as in our previous study on thin films,[39] while the Fermi energy E_F is reduced compared to the value reported in Ref. 39, $E_{F,film} = 0.367$ eV, i.e. we set $E_{F,sphere} = 0.87 \cdot E_{F,film}$ and $E_{F,disk} = 0.79 \cdot E_{F,film}$. This is in agreement with the longer plasma wavelength, and thus lower density of free carriers, of the specific TiN materials constituting the nanosphere and nanodisk samples under consideration. Further insights on the effects of stochiometry of TiN on its band structure, which distinguishes TiN from noble metals, are reported in the SI, Section S3. The change in the electron occupation probability is responsible for a variation of the joint density of states ($\Delta JDOS$) for interband optical transitions to arrival states close to the Fermi level (see Eq. 9, Methods section). This phenomenon relates to the variation of the imaginary part of the interband dielectric permittivity $\Delta\varepsilon''_{IB}(\omega, t)$, which is evaluated by assuming a constant matrix element for the optical transition:[39]

$$\Delta\varepsilon''_{IB}(\omega, t) = \frac{\pi}{3\varepsilon_0}\left(\frac{e}{m_0\omega}\right)^2 |M|^2 \Delta JDOS(\omega, t) \tag{5}$$

where ε_0 is the vacuum permittivity, e and m_0 are, respectively, the free electron charge and mass, and $|M|^2$ is the square matrix element for the transition, considered as a fitting parameter in our model. We set $|M|^2_{disks} = 1.38 \times 10^{-48}$ J kg and $|M|^2_{sphere} = 5.9 \times 10^{-49}$ J kg, not far from the value used for TiN films ($|M|^2_{film} = 3.95 \times 10^{-49}$ J kg).[39] After calculating $\Delta\varepsilon''_{IB}(\omega, t)$, the real part $\Delta\varepsilon'_{IB}(\omega, t)$ can be extracted through Kramers-Kronig transformation. The modulation of the optical properties of TiN upon laser illumination is also caused

by a change in the intraband (Drude-Sommerfeld) part of the permittivity $\Delta\varepsilon_{DS}(\omega,t)$, as an effect of the increment in the lattice temperature T_L. In particular, $\Delta\varepsilon_{DS}(\omega,t)$ relates to two different effects: a major contribution due to the increase in the electron-phonon scattering rate, embedded in the Drude broadening coefficient Γ, and a minor effect owing to the decrease in the plasma frequency ω_P and caused by the volume expansion of the nanostructure upon heating, as described by Eq. 10 and Eq. 11, in the Methods section. This is a major difference with respect to the film's case, where thermoelastic effects come into play.[39] On the contrary, the resonance broadening caused by increased electron-electron collisions is negligible, akin to the films.[39] The two contributions to $\Delta\varepsilon_{DS}$, namely $\Delta\varepsilon_{DS,\Gamma}$ and $\Delta\varepsilon_{DS,\omega_P}$, are reported in Methods section (Eqs. 12 and 13). We can evaluate the variation in the sample's absorbance as:

$$\Delta A(\lambda,t) = -\log_{10}(e^{-\Delta\sigma_{ext}(\lambda,t)N}), \tag{6}$$

where $\Delta\sigma_{ext}(\lambda,t)$ is the modulation of the extinction cross section of the nanoparticle.

The fitting parameters used in the calculations of the transient plasmonic response of TiN nanodisks and nanospheres are summarized in Table 1, compared with the corresponding values exploited in the modelling of TiN films.[39] Despite being chosen so as to best reproduce the experimental results, we highlight that the fitting parameters are all consistent with the literature and with the stationary optical behaviour of TiN nanodisks and nanospheres. This consistency is maintained in the comparison with TiN films.

Fitting parameter	TiN nanodisks	TiN nanospheres	Reference Value (TiN films)
Electron effective mass	$m_{e,disk} = 4\ m_{e,film}$	$m_{e,sphere} = 2\ m_{e,film}$	$m_{e,film} = 1.09 \times 10^{-30}$ kg
Hole effective mass	$m_{h,disk} = 1.2\ m_{e,film}$	$m_{h,sphere} = 1.2\ m_{e,film}$	$m_{h,film} = 6.56 \times 10^{-31}$ kg
Energy gap	$E_{0,disk} = 1.05\ E_{0,film}$	$E_{0,sphere} = 1.05\ E_{0,film}$	$E_{0,film} = 2.8$ eV
Fermi energy	$E_{F,disk} = 0.79\ E_{F,film}$	$E_{F,disk} = 0.87\ E_{F,film}$	$E_{F,film} = 0.367$ eV
Square matrix element of the transition	$\lvert M\rvert^2_{disk} = 3.49\ \lvert M\rvert^2_{film}$	$\lvert M\rvert^2_{sphere} = 1.49\ \lvert M\rvert^2_{film}$	$\lvert M\rvert^2_{film} = 3.95 \times 10^{-49}$ J kg

Table 1: Fitting parameters for the model of TiN nanodisks and nanospheres, compared to the reference values used for TiN films.

The results of our numerical model for nanodisks and nanospheres are reported, respectively, in Figs. 2b and 2d. In the case of nanodisks, the pump fluence is set to 2.25 mJ cm^{-2} in the simulations, close to the experimental value. For the nanospheres, the fluence is kept as a fitting parameter, since not provided in the original paper[37] and set to 336 μJ cm^{-2}. Our simulations reproduce with remarkable precision the experimental results previously published, both in time and on a broad range of wavelengths. The agreement is achieved also for minor, ultrafast features of the transient spectra. Especially, the negative signal tail at ∼1150 nm and the positive contribution at shorter wavelengths, both taking place in the first instants of the nanodisk dynamics (Fig. 2a), are precisely replicated by our numerical model (Fig. 2b).

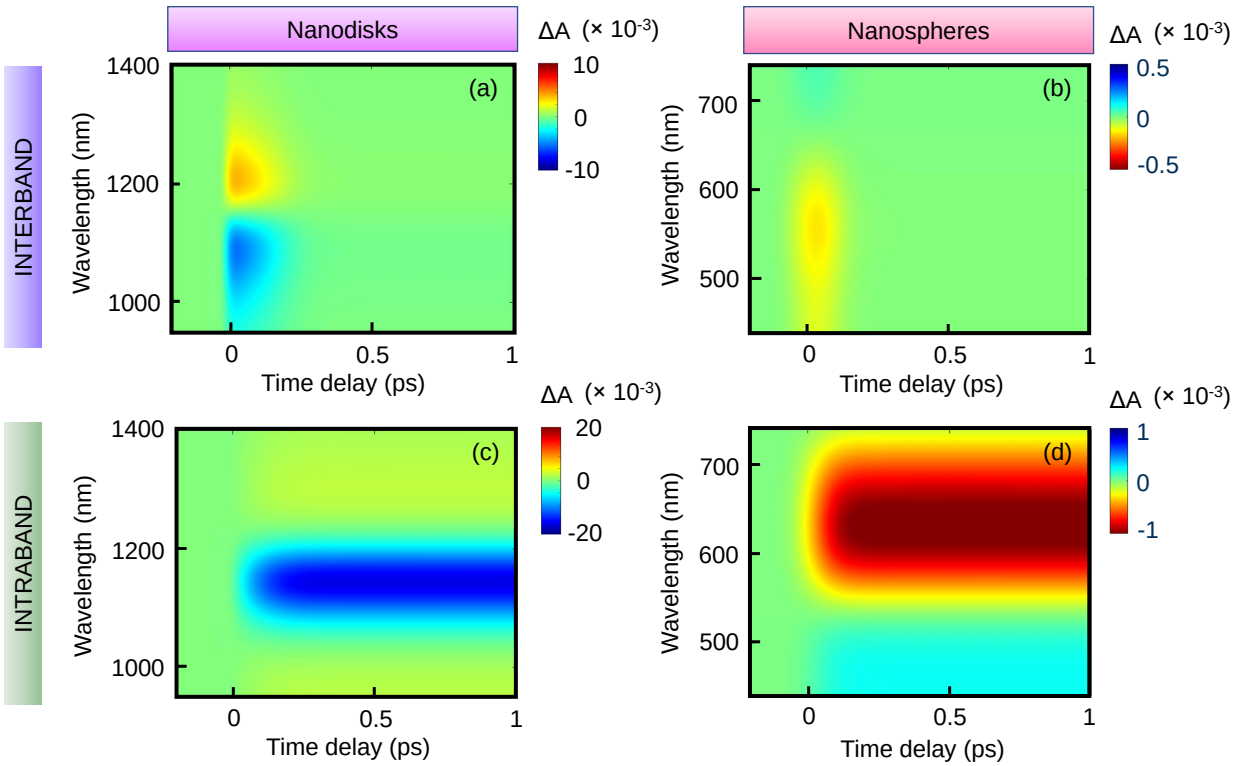

Figure 4: Disentanglement of the a)-b) interband and c)-d) intraband parts of the transient optical response of nanodisks (panels a) and c)) and nanospheres (panels b) and d)). The color scale in panels a) and b) is decreased by a factor of 2 compared to c) and d), respectively, for better visualization.

In addition, our numerical model enables us to disentangle the transient interband and

intraband contributions to the samples' transient optical absorbance. In Fig. 4, we present the absorbance variation generated separately by the modulation of the interband (Figs. 4a and 4b) or intraband (Figs. 4c and 4d) part of the permittivity only, both for nanodisks (Figs. 4a and 4c) and for nanospheres (Figs. 4b and 4d). Starting with the interband optical response of nanodisks, we find a double lobe, with the negative part extending over the short wavelength range of the spectrum (see Fig. 4a). This contribution only lasts for the first ∼250 fs after the arrival of the pump pulse. Interestingly, we note from Fig. 4c that, by switching off the interband permittivity modulation, we completely loose the features at short time delays (< ∼250 fs) that characterize the transient optical response of nanodisks (see the comparison between experiment and model in Figs. 2a and 2b). Indeed, this evidences that $\Delta\varepsilon_{IB}$ is responsible for the short-living plasmon red-shift (anti-symmetric spectral profile of ΔA), while $\Delta\varepsilon_{DS}$ results in plasmon damping and broadening, lasting for longer temporal delays. As such, the Drude-Sommerfeld contribution itself is not sufficient to accurately predict the modulation of the optical properties of TiN nanodisks in the ultrafast temporal regime. On the contrary, for nanospheres, the disentanglement of the interband and intraband contributions to ΔA shows a different result. Indeed, the interband modulation extends up to ∼200 fs, but its intensity is rather low compared to the intraband counterpart (also note that colorscales in Figs. 4a and 4b are reduced for clarity). In this case, the effect of the Fermi smearing on the overall optical response is negligible, and the main features of the experiment's spectral dynamics can be entirely reproduced by including the modulation of the Drude-Sommerfeld permittivity only. Interestingly, our numerical model enables us to disclose in a clear-cut way the connection between the spectral features observed in the ultrafast optical response and the plasmonic resonances found in the stationary spectra of nanodisks (at ∼1150 nm and ∼460 nm) and nanospheres (at ∼625 nm). In Figs. 5a-d, we display the real and imaginary parts of the permittivity variation arising from interband transition modulation, $\Delta\varepsilon_{IB}$ (dark curves), and from the Drude-Sommerfeld modulation, $\Delta\varepsilon_{DS}$ (light curves), for nanodisks (Figs. 5a,c) and for nanospheres (Figs. 5b,d) on a broad

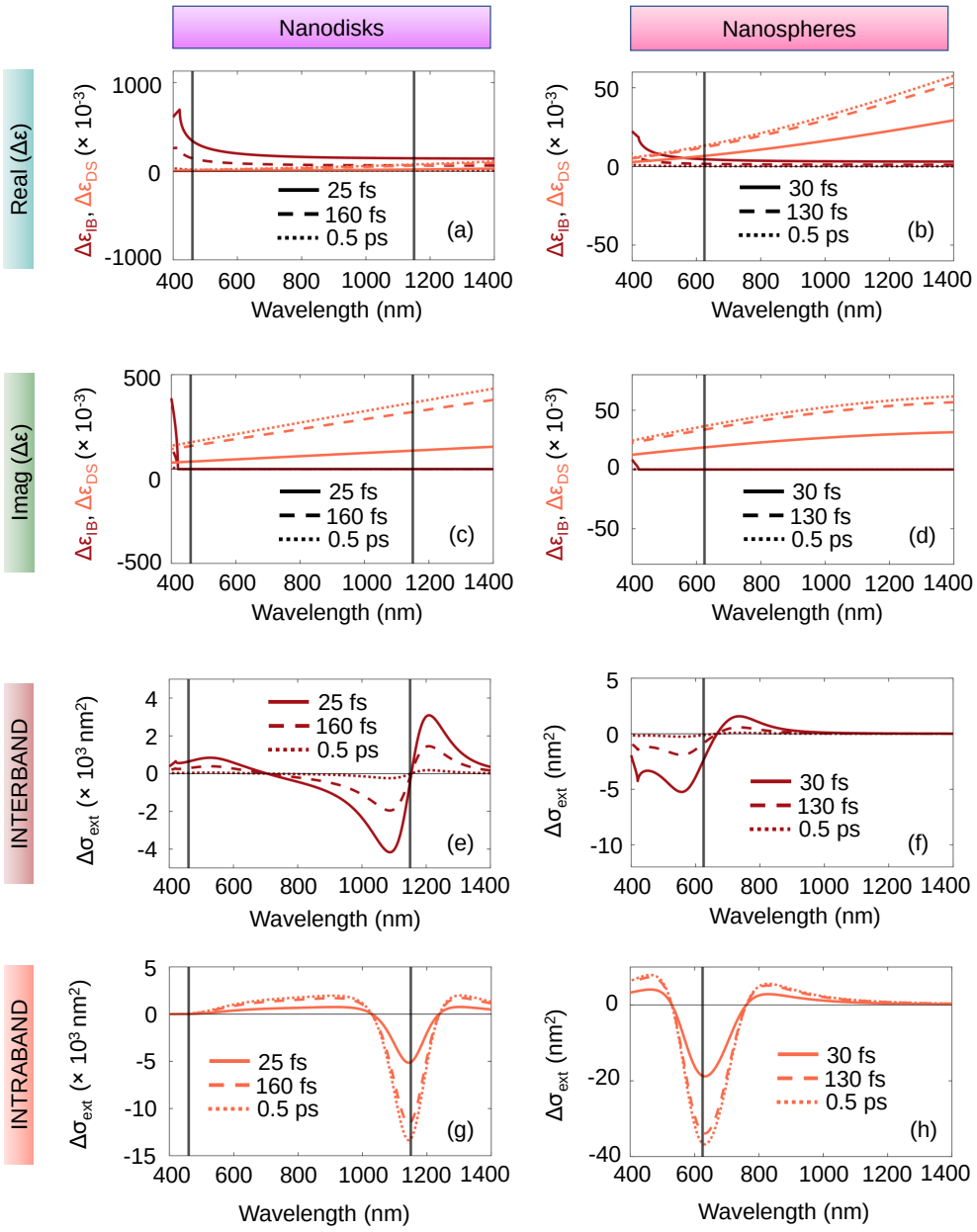

Figure 5: (a)-(b) Real and (c)-(d) imaginary parts of the interband (dark red curves) and intraband (orange curves) permittivity modulation, for nanodisks [(a) and (c)] and nanospheres [(b) and (d)]. (e)-(h) Disentanglement of the modulation of the extinction cross section taking into account only the interband [(e)-(f)] or the intraband [(g)-(h)] contribution to $\Delta\varepsilon$, for nanodisks [(e) and (g)] and nanospheres [(f) and (h)]. All modulations are displayed at different time delays following pump excitation, namely at the peak of the carrier temperature (solid curve), at half of its decay (dashed curve), and after the increase of the lattice temperature (dotted curve). Vertical black lines mark the spectral position of the plasmonic resonances in the stationary spectra of Fig. 1.

spectral range and at three different temporal delays after the pump interaction with the sample. These delays refer to: the peak of the carrier temperature, half of its decay, and the complete thermalization between electrons and lattice, corresponding to $t_1 = 25$ fs, $t_2 = 160$ fs and $t_3 = 0.5$ ps for nanodisks, and $t_1 = 30$ fs, $t_2 = 130$ fs and $t_3 = 0.5$ ps for nanospheres, respectively. Note that the interband contribution to the permittivity modulation (both real and imaginary parts) is strongly dispersed in wavelength, with a strong contribution at about 400 nm, i.e., close to a probe photon energy $E_{ph} = E_0 + E_F$ around which the Fermi smearing is more pronounced. The Drude-Sommerfeld contribution has instead an almost negligible dispersion over the whole spectral range. For probe wavelengths corresponding to $E_{ph} > E_0$ (the bandgap energy of the considered transition), i.e., for wavelengths $\lambda > 420$ nm (for both nanostructures), the $\Delta\varepsilon_{IB}$ is narrowed down to its real part. Finally, when comparing Figs. 5a,c with Figs. 5b,d we note a slight difference between the permittivity modulations predicted for the nanodisks and for the nanospheres. This difference reflects, first of all, the different nitrogen content in the TiN material employed for the two structures, that has an impact on the optical parameters of the medium, as already stated above, and also the different excitation levels of the two nanostructured systems (mostly responsible for the quantitative differences in $\Delta\varepsilon$).

From $\Delta\varepsilon_{IB}$ and $\Delta\varepsilon_{DS}$ we can disentangle the mechanisms presiding over the extinction cross section variation, $\Delta\sigma_{ext}$, entering Eq. 6. In the perturbative regime of modulation taking place in the considered experiments, $\Delta A \propto \Delta\sigma_{ext}$, as per Eq. 6. So, all the following considerations on the $\Delta\sigma_{ext}$ apply to the ΔA. The calculated $\Delta\sigma_{ext}$ is displayed in Figs. 5e,g for nanodisks, and in Figs. 5f,h for nanospheres, disentangled in terms of interband (Figs. 5e,f) and intraband (Figs. 5g,h) contributions.

Regarding the predicted spectral shape of $\Delta\sigma_{ext}$ for nanodisks, note that the modulation arising from the interband contribution (Fig. 5e) is dominated by a derivative-shaped spectrum around to the plasmonic resonance at $\lambda \sim 1150$ nm. This behavior is ascribable to the positive sign of the real $\Delta\varepsilon_{IB}$ (dark curves in Fig. 5a) which is known to induce a red

shift of plasmonic resonances when these are not overlapping with interband transitions.[50] On the contrary, the $\Delta\sigma_{ext}$ from Drude-Sommerfeld permittivity modulation (Fig. 5g) exhibits a characteristic shape streaming from the broadening of the plasmonic resonance, with a strong negative central lobe and two weaker positive lobes at longer and shorter wavelengths. This is consistent with the fact that $\Delta\varepsilon_{DS}$ (light curves in Fig. 5a and 5c) involves a sizable increase in the imaginary permittivity, meaning an increase in absorption losses. For what concerns the weaker mode at $\lambda \sim 460$ nm, it is detuned from $E_0 + E_F$ ($\lambda \sim 383$ nm) and it is much weaker compared to the main mode in the infrared. These properties lower the system sensitivity to the permittivity change. Therefore, despite the huge permittivity modulation in the spectral range below 420 nm, $\Delta\sigma_{ext}$ turns out to be very low in the visible (see Fig. 5e). Similarly, for nanospheres, looking at the spectral shape of $\Delta\sigma_{ext}$, we also notice the red shift arising from $\Delta\varepsilon_{IB}$ (Fig. 5f) and the broadening of the plasmonic resonance, here sitting at ~ 625 nm, arising from $\Delta\varepsilon_{DS}$ (Fig. 5h). Regarding the latter, it is worth saying that despite its sizable growth with the probe wavelength, the impact of the $\Delta\varepsilon_{DS}$ on the transient extinction spectrum actually becomes lower and lower for longer wavelengths, contrary to the case of the $\Delta\varepsilon_{IB}$. This is evident when normalizing the $\Delta\varepsilon_{IB}$ and the $\Delta\varepsilon_{DS}$ to the stationary ε_{IB} and ε_{DS} permittivity, respectively (see supporting Figure S3). The reason behind this behaviour is that the stationary ε_{DS} also grows with wavelength, whereas the stationary ε_{IB} is weakly dispersed in the considered wavelength range.

As for the temporal behavior of $\Delta\sigma_{ext}$, we disclose a distinct response for nanodisks and nanospheres. For the former, the interband contribution dominates over the intraband one in the first tens of fs of the electron dynamics. After ~160 fs, even though it is still non-zero, the interband component of $\Delta\sigma_{ext}$ is significantly lower compared with the intraband one, which has already approached the value corresponding to the temperature plateau (see Fig. 5e). Therefore, at increasing time delays after pump excitation, the monotonic decrease of the interband part of $\Delta\sigma_{ext}$ is counterbalanced by the monotonic increase in the magnitude of the

intraband one. On the contrary, for nanospheres, the interband contribution never exceeds the Drude-Sommerfeld one in the spectral range considered in the pump-probe experiment, not even at the early stages of the dynamics. As evident from Figs. 5f and 5h, either the two contributions to $\Delta\sigma_{ext}$ are comparable (e.g., at ∼30 fs and λ ∼450 nm) or intraband contribution is larger (see, e.g., $\Delta\sigma_{ext}$ at λ ∼500 nm). As the dynamics progresses, the temporal evolution mirrors the one observed in nanodisks.

Conclusions

In conclusion we modeled the permittivity modulation of TiN nanostructures in the transient regime upon photoexcitation with fs-laser pulses. We show that, to correctly simulate the ultrafast optical response of TiN plasmonic nanostructures, it is possibile to use the same approach proposed for TiN films, yet it is necessary to tailor part of the calculations to suit the different sample configurations. Specifically, it is crucial to introduce the effect of heat dissipation towards the environment, besides the nanostructure geometrically-induced resonant behaviour, and it is licit to neglect both electron and phonon diffusion. To validate our theoretical approach, we selected a lattice of TiN nanodisks on glass and a colloidal solution of TiN nanospheres in water, which are rather representative cases and have been previously studied by other groups through ultrafast pump-probe spectroscopy.[36,37] We provided a theoretical understanding of the ultrarapid relaxation of the hot carriers and their interaction with the lattice, which was still lacking in the previous studies. By combining a two-temperature model for the hot carrier dynamics and a semiclassical description of optical transitions in TiN, we evaluated the modulation of the interband and intraband contributions to the TiN dielectric permittivity, both in time and on a broad spectral domain. Thanks to the disentanglement of the contributions to the modulation of the TiN dielectric function, we revealed the physical origin of the response for the two nanostructured systems, and we pointed out the key role of the Fermi smearing at the interband transition around the Γ point in the optical response of TiN nanodisks on the ultrashort (<200 fs) temporal regime.

We proved that our numerical model, initially developed for a TiN film,[39] is a powerful tool for the comprehensive and accurate understanding of the transient optical response of TiN nanostructures. Overall, our work provides the basis for the design of TiN-based nanomaterials and systems with tailored properties in the ultrafast regime, being greatly beneficial in view of future technological applications.

Methods

Numerical modeling

The extinction and scattering cross sections of the TiN nanoparticles are calculated from the polarizability as follows:[44]

$$\sigma_{ext}(\lambda) = \frac{8\pi^2}{\sqrt{\varepsilon_h}\lambda}\mathrm{Im}\{\alpha(\lambda)\} \tag{7}$$

$$\sigma_{scat}(\lambda) = \frac{128\pi^5}{3\lambda^4}|\alpha(\lambda)|^2 \tag{8}$$

where λ is the probe wavelength and ε_h is the dielectric permittivity of the host medium. For nanodisks, ε_h is retrieved as a mean value from the refractive indexes of sapphire $n_{sapph} = 1.75$ and air $n_{air} = 1$ as $\varepsilon_h = p \cdot \sqrt{(n_{sapph}^2 + n_{air}^2)/2}$, with a scale factor $p = 0.945$ which takes into account the bigger amount of air with respect to sapphire around the nanodisks. The modulation in the JDOS induced by the Fermi smearing can be explicited, for a specific transition and under parabolic bands approximation, as:[49,51]

$$\Delta JDOS(\omega, t) = -\frac{2}{4\pi^2}\left(\frac{2m_r}{\hbar^2}\right)^{3/2}\sqrt{\hbar\omega - E_0} \times \Delta f(E_\omega, t). \tag{9}$$

In the equation above, $\hbar$ is the reduced Planck constant, c is the light speed in vacuum and ω is the probe angular frequency. The reduced mass of the system $m_r = m_e m_h/(m_e + m_h)$ is calculated from the effective masses m_e of the electrons and m_h of the holes, and $E_\omega = m_r/m_e(\hbar\omega - E_0) - E_F$.

The modifications in the Drude damping factor Γ and the decrease in the plasma frequency ω_P are computed as follows:

$$\Delta\Gamma(\omega, t) = b(\hbar\omega)^2(T_L(t) - T_0) \tag{10}$$

$$\Delta\omega_P(t) = -\frac{1}{2}\frac{\omega_P}{V}\Delta V(t). \tag{11}$$

In the equations above, V is the nanoparticle volume and $b = 1.17 \times 10^{49}\mathrm{J}^{-2}\ \mathrm{K}^{-1}\ \mathrm{s}^{-1}$ is the electron-phonon damping coefficient, for both nanodisks and nanospheres, and its value is higher than the one used for TiN films, but of the same order of magnitude.[39] With these results, we can find the corresponding modulations of the Drude-Sommerfeld permittivity as follows:

$$\Delta\varepsilon_{DS,\Gamma}(\omega, t) = \frac{\mathrm{i}\omega_P^2\Delta\Gamma(\omega, t)}{\omega(\omega + \mathrm{i}\Gamma)[\omega + \mathrm{i}\Gamma + \mathrm{i}\Delta\Gamma(\omega, t)]}, \tag{12}$$

$$\Delta\varepsilon_{DS,\omega_P}(\omega, t) = -\frac{\Delta\omega_P(t)[\Delta\omega_P(t) + 2\omega_P]}{\omega(\omega + \mathrm{i}\Gamma)}. \tag{13}$$

Finally, the total variation of the Drude-Sommerfeld permittivity can be calculated as:

$$\Delta\varepsilon_{DS}(\omega, t) = \Delta\varepsilon_{DS,\Gamma}(\omega, t) + \Delta\varepsilon_{DS,\omega_P}(\omega, t). \tag{14}$$

Funding Sources

This publication is part of the METAFAST project that received funding from the European Union Horizon 2020 Research and Innovation programme under Grant Agreement No.899673. This work reflects only author view and the European Commission is not responsible for any use that may be made of the information it contains.

S.R.L. acknowledges the 5 months funding from "Bourse internationale ENS Paris-Saclay 2022 – 2023". G.D.V. and S.R.L. acknowledge support from the HOTMETA project under the PRIN 2022 MUR program funded by the European Union – Next Generation EU

- "PNRR - M4C2, investimento 1.1 - "Fondo PRIN 2022" - HOT-carrier METasurfaces for Advanced photonics (HOTMETA), contract no. 2022LENW33 - CUP: D53D2300229 0006". A.S., and G.D.V. acknowledge financial support by the European Union's NextGenerationEU Programme with the I-PHOQS Infrastructure [IR0000016, ID D2B8D520, CUP B53C22001750006] "Integrated infrastructure initiative in Photonic and Quantum Sciences".

Supporting Information Available

Supporting Information for this work is provided. The following files are available free of charge at https://pubs.acs.org/.

- Stationary permittivity of TiN nanodisks and nanospheres: numerical constants for the permittivity;
- Figure S1: stationary permittivity of TiN a) nanodisks and b) nanospheres;
- Absorbed pump power density: formula for the pump power absorbed per unit volume by the sample.
- $\Delta\varepsilon$ normalization plots: plots of real and imaginary parts of the interband and Drude-Sommerfeld permittivity modulation, normalized to the respective real and imaginary stationary permittivities.

References

(1) Liu, J.; He, H.; Xiao, D.; Yin, S.; Ji, W.; Jiang, S.; Luo, D.; Wang, B.; Liu, Y. Recent advances of plasmonic nanoparticles and their applications. *Materials* **2018**, *11*, 1833.

(2) Butet, J.; Yang, K.-Y.; Dutta-Gupta, S.; Martin, O. J. Maximizing nonlinear optical conversion in plasmonic nanoparticles through ideal absorption of light. *ACS Photonics* **2016**, *3*, 1453–1460.

(3) Gwo, S.; Wang, C.-Y.; Chen, H.-Y.; Lin, M.-H.; Sun, L.; Li, X.; Chen, W.-L.; Chang, Y.-M.; Ahn, H. Plasmonic metasurfaces for nonlinear optics and quantitative SERS. *ACS Photonics* **2016**, *3*, 1371–1384.

(4) Krasavin, A. V.; Ginzburg, P.; Zayats, A. V. Free-electron optical nonlinearities in plasmonic nanostructures: a review of the hydrodynamic description. *Laser & Photonics Reviews* **2018**, *12*, 1700082.

(5) Zavelani-Rossi, M.; Polli, D.; Kochtcheev, S.; Baudrion, A.-L.; Béal, J.; Kumar, V.; Molotokaite, E.; Marangoni, M.; Longhi, S.; Cerullo, G. et al. Transient optical response of a single gold nanoantenna: the role of plasmon detuning. *ACS Photonics* **2015**, *2*, 521–529.

(6) Brongersma, M. L.; Halas, N. J.; Nordlander, P. Plasmon-induced hot carrier science and technology. *Nature Nanotechnology* **2015**, *10*, 25–34.

(7) Del Fatti, N.; Vallée, F.; Flytzanis, C.; Hamanaka, Y.; Nakamura, A. Electron dynamics and surface plasmon resonance nonlinearities in metal nanoparticles. *Chemical Physics* **2000**, *251*, 215–226.

(8) Besteiro, L. V.; Yu, P.; Wang, Z.; Holleitner, A. W.; Hartland, G. V.; Wiederrecht, G. P.; Govorov, A. O. The fast and the furious: Ultrafast hot electrons in plasmonic metastructures. Size and structure matter. *Nano Today* **2019**, *27*, 120–145.

(9) Schirato, A.; Maiuri, M.; Cerullo, G.; Della Valle, G. Ultrafast hot electron dynamics in plasmonic nanostructures: experiments, modelling, design. *Nanophotonics* **2023**, *12*, 1–28.

(10) Wang, X.; Guillet, Y.; Selvakannan, P. R.; Remita, H.; Palpant, B. Broadband spectral signature of the ultrafast transient optical response of gold nanorods. *The Journal of Physical Chemistry C* **2015**, *119*, 7416–7427.

(11) Harutyunyan, H.; Martinson, A. B.; Rosenmann, D.; Khorashad, L. K.; Besteiro, L. V.; Govorov, A. O.; Wiederrecht, G. P. Anomalous ultrafast dynamics of hot plasmonic electrons in nanostructures with hot spots. *Nature nanotechnology* **2015**, *10*, 770–774.

(12) Naik, G. V.; Shalaev, V. M.; Boltasseva, A. Alternative plasmonic materials: beyond gold and silver. *Advanced Materials* **2013**, *25*, 3264–3294.

(13) Guler, U.; Naik, G. V.; Boltasseva, A.; Shalaev, V. M.; Kildishev, A. V. Performance analysis of nitride alternative plasmonic materials for localized surface plasmon applications. *Applied Physics B* **2012**, *107*, 285–291.

(14) Guler, U.; Shalaev, V. M.; Boltasseva, A. Nanoparticle plasmonics: going practical with transition metal nitrides. *Materials Today* **2015**, *18*, 227–237.

(15) Yang, Z.-Y.; Ishii, S.; Doan, A. T.; Shinde, S. L.; Dao, T. D.; Lo, Y.-P.; Chen, K.-P.; Nagao, T. Narrow-Band Thermal Emitter with Titanium Nitride Thin Film Demonstrating High Temperature Stability. *Advanced Optical Materials* **2020**, *8*, 1900982.

(16) Krekeler, T.; Rout, S. S.; Krishnamurthy, G. V.; Störmer, M.; Arya, M.; Ganguly, A.; Sutherland, D. S.; Bozhevolnyi, S. I.; Ritter, M.; Pedersen, K. et al. Unprecedented thermal stability of plasmonic titanium nitride films up to 1400° C. *Advanced Optical Materials* **2021**, *9*, 2100323.

(17) Roberts, A. S.; Chirumamilla, M.; Wang, D.; An, L.; Pedersen, K.; Mortensen, N. A.; Bozhevolnyi, S. I. Ultra-thin titanium nitride films for refractory spectral selectivity. *Optical Materials Express* **2018**, *8*, 3717–3728.

(18) Kharitonov, A.; Kharintsev, S. Tunable optical materials for multi-resonant plasmonics: from TiN to TiON. *Optical Materials Express* **2020**, *10*, 513–531.

(19) Li, W.; Guler, U.; Kinsey, N.; Naik, G. V.; Boltasseva, A.; Guan, J.; Shalaev, V. M.;

Kildishev, A. V. Refractory plasmonics with titanium nitride: broadband metamaterial absorber. *Advanced Materials* **2014**, *26*, 7959–7965.

(20) Chirumamilla, M.; Chirumamilla, A.; Yang, Y.; Roberts, A. S.; Kristensen, P. K.; Chaudhuri, K.; Boltasseva, A.; Sutherland, D. S.; Bozhevolnyi, S. I.; Pedersen, K. Large-area ultrabroadband absorber for solar thermophotovoltaics based on 3D titanium nitride nanopillars. *Advanced Optical Materials* **2017**, *5*, 1700552.

(21) Chernykh, E. A.; Filippov, A. N.; Alekseev, A. M.; Makhiboroda, M. A.; Kharintsev, S. S. Optical Heating Controlled With a Thermoplasmonic Metasurface. *Journal of Physics: Conference Series* **2021**, *2015*, 012029.

(22) Kharintsev, S. S.; Kharitonov, A. V.; Chernykh, E. A.; Alekseev, A. M.; Filippov, N. A.; Kazarian, S. G. Designing two-dimensional temperature profiles using tunable thermoplasmonics. *Nanoscale* **2022**, *14*, 12117–12128.

(23) Mascaretti, L.; Schirato, A.; Zbořil, R.; Kment, Š.; Schmuki, P.; Alabastri, A.; Naldoni, A. Solar steam generation on scalable ultrathin thermoplasmonic TiN nanocavity arrays. *Nano Energy* **2021**, *83*, 105828.

(24) Zhang, J.; Hu, H.; Liu, X.; Li, D.-S. Development of the applications of titanium nitride in fuel cells. *Materials today chemistry* **2019**, *11*, 42–59.

(25) Naldoni, A.; Kudyshev, Z. A.; Mascaretti, L.; Sarmah, S. P.; Rej, S.; Froning, J. P.; Tomanec, O.; Yoo, J. E.; Wang, D.; Kment, S. et al. Solar thermoplasmonic nanofurnace for high-temperature heterogeneous catalysis. *Nano Letters* **2020**, *20*, 3663–3672.

(26) Gao, B.; Li, X.; Ding, K.; Huang, C.; Li, Q.; Chu, P. K.; Huo, K. Recent progress in nanostructured transition metal nitrides for advanced electrochemical energy storage. *Journal of Materials Chemistry A* **2019**, *7*, 14–37.

(27) Qin, P.; Li, X.; Gao, B.; Fu, J.; Xia, L.; Zhang, X.; Huo, K.; Shen, W.; Chu, P. K. Hierarchical TiN nanoparticles-assembled nanopillars for flexible supercapacitors with high volumetric capacitance. *Nanoscale* **2018**, *10*, 8728–8734.

(28) Ifijen, I. H.; Maliki, M. A comprehensive review on the synthesis and photothermal cancer therapy of titanium nitride nanostructures. *Inorganic and Nano-Metal Chemistry* **2023**, *53*, 366–387.

(29) Rajesh, Y.; Bharati, M.; Rao, S. V.; Krishna, M. G. ZnO nanowire arrays decorated with titanium nitride nanoparticles as surface-enhanced Raman scattering substrates. *Applied Physics A* **2021**, *127*, 1–8.

(30) Gosciniak, J.; Justice, J.; Khan, U.; Corbett, B. Study of TiN nanodisks with regard to application for Heat-Assisted Magnetic Recording. *MRS Advances* **2016**, *1*, 317–326.

(31) Patsalas, P.; Kalfagiannis, N.; Kassavetis, S. Optical properties and plasmonic performance of titanium nitride. *Materials* **2015**, *8*, 3128–3154.

(32) Cortie, M.; Giddings, J.; Dowd, A. Optical properties and plasmon resonances of titanium nitride nanostructures. *Nanotechnology* **2010**, *21*, 115201.

(33) Guler, U.; Suslov, S.; Kildishev, A. V.; Boltasseva, A.; Shalaev, V. M. Colloidal plasmonic titanium nitride nanoparticles: properties and applications. *Nanophotonics* **2015**, *4*, 269–276.

(34) Ern, V.; Switendick, A. Electronic band structure of TiC, TiN, and TiO. *Physical Review* **1965**, *137*, A1927.

(35) Sato, R.; Ishii, S.; Nagao, T.; Naito, M.; Takeda, Y. Broadband plasmon resonance enhanced third-order optical nonlinearity in refractory titanium nitride nanostructures. *ACS Photonics* **2018**, *5*, 3452–3458.

(36) Reese, T.; Reed, A. N.; Sample, A. D.; Freire-Fernández, F.; Schaller, R. D.; Urbas, A. M.; Odom, T. W. Ultrafast spectroscopy of plasmonic titanium nitride nanoparticle lattices. *ACS Photonics* **2021**, *8*, 1556–1561.

(37) Adhikari, S.; Cortes, C. L.; Wen, X.; Panuganti, S.; Gosztola, D. J.; Schaller, R. D.; Wiederrecht, G. P.; Gray, S. K. Accelerating ultrafast spectroscopy with compressive sensing. *Physical Review Applied* **2021**, *15*, 024032.

(38) Diroll, B. T.; Saha, S.; Shalaev, V. M.; Boltasseva, A.; Schaller, R. D. Broadband ultrafast dynamics of refractory metals: TiN and ZrN. *Advanced Optical Materials* **2020**, *8*, 2000652.

(39) Rotta Loria, S.; Bricchi, B. R.; Schirato, A.; Mascaretti, L.; Mancarella, C.; Naldoni, A.; Li Bassi, A.; Della Valle, G.; Zavelani-Rossi, M. Unfolding the Origin of the Ultrafast Optical Response of Titanium Nitride. *Advanced Optical Materials* **2023**, 2300333.

(40) Shcherbakov, M. R.; Vabishchevich, P. P.; Shorokhov, A. S.; Chong, K. E.; Choi, D.-Y.; Staude, I.; Miroshnichenko, A. E.; Neshev, D. N.; Fedyanin, A. A.; Kivshar, Y. S. Ultrafast all-optical switching with magnetic resonances in nonlinear dielectric nanostructures. *Nano letters* **2015**, *15*, 6985–6990.

(41) Della Valle, G.; Polli, D.; Biagioni, P.; Martella, C.; Giordano, M.; Finazzi, M.; Longhi, S.; Duo, L.; Cerullo, G.; de Mongeot, F. B. Self-organized plasmonic metasurfaces for all-optical modulation. *Physical Review B* **2015**, *91*, 235440.

(42) Taghinejad, M.; Cai, W. All-optical control of light in micro-and nanophotonics. *Acs Photonics* **2019**, *6*, 1082–1093.

(43) Crotti, G.; Schirato, A.; Zaccaria, R. P.; Della Valle, G. On the limits of quasi-static theory in plasmonic nanostructures. *Journal of Optics* **2021**, *24*, 015001.

(44) Yu, R.; Liz-Marzán, L. M.; de Abajo, F. J. G. Universal analytical modeling of plasmonic nanoparticles. *Chemical Society Reviews* **2017**, *46*, 6710–6724.

(45) Allen, P. B. Theory of thermal relaxation of electrons in metals. *Physical review letters* **1987**, *59*, 1460.

(46) Mazzanti, A.; Yang, Z.; Silva, M. G.; Yang, N.; Rizza, G.; Coulon, P.-E.; Manzoni, C.; de Paula, A. M.; Cerullo, G.; Della Valle, G. et al. Light–heat conversion dynamics in highly diversified water-dispersed hydrophobic nanocrystal assemblies. *Proceedings of the National Academy of Sciences* **2019**, *116*, 8161–8166.

(47) Dal Forno, S.; Lischner, J. Electron-phonon coupling and hot electron thermalization in titanium nitride. *Physical Review Materials* **2019**, *3*, 115203.

(48) Schirato, A.; Crotti, G.; Gonçalves Silva, M.; Teles-Ferreira, D. C.; Manzoni, C.; Proietti Zaccaria, R.; Laporta, P.; de Paula, A. M.; Cerullo, G.; Della Valle, G. Ultrafast plasmonics beyond the perturbative regime: Breaking the electronic-optical dynamics correspondence. *Nano Letters* **2022**, *22*, 2748–2754.

(49) Rosei, R. Temperature modulation of the optical transitions involving the Fermi surface in Ag: Theory. *Physical Review B* **1974**, *10*, 474.

(50) Schirato, A.; Silva, M. G.; Teles-Ferreira, D. C.; Manzoni, C.; de Paula, A. M.; Cerullo, G.; Della Valle, G.; Di Vece, M. Disentangling the Ultrafast Nonlinear Optical Behavior of Plasmonic Resonances Near the Interband Transition. *Advanced Photonics Research* **2023**, *4*, 2200081.

(51) Marini, A.; Conforti, M.; Della Valle, G.; Lee, H.; Tran, T. X.; Chang, W.; Schmidt, M. A.; Longhi, S.; Russell, P. S. J.; Biancalana, F. Ultrafast nonlinear dynamics of surface plasmon polaritons in gold nanowires due to the intrinsic nonlinearity of metals. *New Journal of Physics* **2013**, *15*, 013033.

TOC Graphic